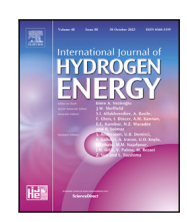
\$ 50 CONTRACTOR OF THE SECOND SECOND

Contents lists available at ScienceDirect

# International Journal of Hydrogen Energy

journal homepage: www.elsevier.com/locate/he





# Electrochemical and microstructure study of ceramic composite based on $BaCo_{0.4}Fe_{0.4}Zr_{0.2} O_{3-\delta}$ : $BaZr_{0.7}Ce_{0.2}Y_{0.1}O_{3-\delta}$ as a steam electrode interlayer in proton-conducting electrolysis cells

Shivam Kumar Dwivedi <sup>a,b</sup>, Yuan Zeng <sup>b,c</sup>, Laura-Alena Schaefer <sup>b,c</sup>, Muhammad Shirjeel Khan b, Kwati Leonard d, Norbert H. Menzler b,c, Olivier Guillon b,c,e, Mariya E. Ivanova b, \*, Ravi Kumar a,e, \*, Ravi Kumar a,e,

- <sup>a</sup> Laboratory for High Performance Ceramics, Department of Metallurgical and Materials Engineering, Indian Institute of Technology-Madras (IIT Madras), Chennai, 600036, India
- b Institute of Energy Materials and Devices Materials Synthesis and Processing (IMD-2), Forschungszentrum Jülich GmbH, Jülich, 52428, Germany
- c Department of Ceramics and Refractory Materials, Institute of Mineral Engineering, RWTH Aachen University, Aachen, 52078, Germany
- <sup>d</sup> Center for Energy System Design, International Institute for Carbon-Neutral Energy Research (I2CNER) Kyushu University, 744 Motooka, Nishi-ku, Fukuoka, 819-0395, Japan
- <sup>e</sup> Research Center on Ceramic Technologies for Futuristic Mobility, Institute of Eminence (IoE), Indian Institute of Technology-Madras (IIT Madras), Chennai, 600036, India

#### ARTICLE INFO

# Keywords: Proton-conducting ceramic electrolysis cells Steam electrode Ceramic-ceramic composites Electrochemical analysis Screen printing

#### ABSTRACT

A primary challenge in advancing proton-conducting electrolysis cells for  $H_2$  generation lies in enhancing the performance and durability of the steam electrode. This paper addresses common delamination issues, frequently observed during cell operation due to thermal expansion mismatch, by introducing a novel functional layer — an intermediate component intended to be placed between the steam electrode and the electrolyte. We systematically investigate the optimal composition of this functional layer, based on  $BaCo_{0.4}Fe_{0.4}Zr_{0.2}O_{3-\delta}$  (BCFZ442)/BaZr $_{0.7}Ce_{0.2}Y_{0.1}O_{3-\delta}$  (BZCY721), alongside its associated ink rheology. The electrochemical performance of the composite functional layer is comprehensively assessed on symmetrical cells under humidified air within the temperature range of 200 to 700 °C. Furthermore, detailed microstructural analyses are conducted before and after cell operation to provide critical insights for future improvements. The study also explores the impact of layer thickness, influenced by varying ethyl cellulose (EC) binder weight fractions, on the area-specific resistance (ASR). The BCFZ: BZCY (70:30) composite, prepared with 3 wt% EC, demonstrates the lowest area-specific resistance of 0.99  $\Omega$ cm² and an activation energy of 0.94 eV at 600 °C. These findings suggest that the developed composite maintains optimal charge transfer kinetics and conductivity, simultaneously preventing delamination.

# 1. Introduction

Achieving carbon neutrality and large-scale energy storage remains a critical challenge for modern society. Hydrogen  $(H_2)$ , a versatile chemical energy carrier with high energy density, offers an attractive solution for sustainable energy systems. Among the leading technologies for hydrogen production, Solid Oxide Electrolysis (SOE) presents distinct advantages in terms of efficiency and integration potential, distinguishing it from both Proton Exchange Membrane (PEM) electrolysis [1] and Photoelectrocatalysis (PEC) [2]. While PEC represents a

long-term research pathway that directly uses sunlight to split water, it currently faces significant challenges such as low solar-to-hydrogen efficiency and fast charge recombination, making it unsuitable for large-scale, commercial applications in the near term. In contrast, PEM electrolysis is a commercially mature technology with a high current density and the ability to respond rapidly to the intermittent nature of renewable energy sources. However, PEM systems rely on expensive precious metals like platinum and iridium, which significantly drives up their capital cost.SOE presents a highly promising route for

https://doi.org/10.1016/j.ijhydene.2025.151426

Received 17 April 2025; Received in revised form 4 September 2025; Accepted 7 September 2025 Available online 19 September 2025

<sup>\*</sup> Corresponding authors.

E-mail addresses: dwivedis@alumni.iitm.ac.in (S.K. Dwivedi), y.zeng@fz-juelich.de (Y. Zeng), mariya.e.ivanova@takia-uni.bg (M.E. Ivanova), nyrk@iitm.ac.in (R. Kumar).

Present affiliation: Trakia University, Students Campus, Stara Zagora, 6000, Bulgaria.

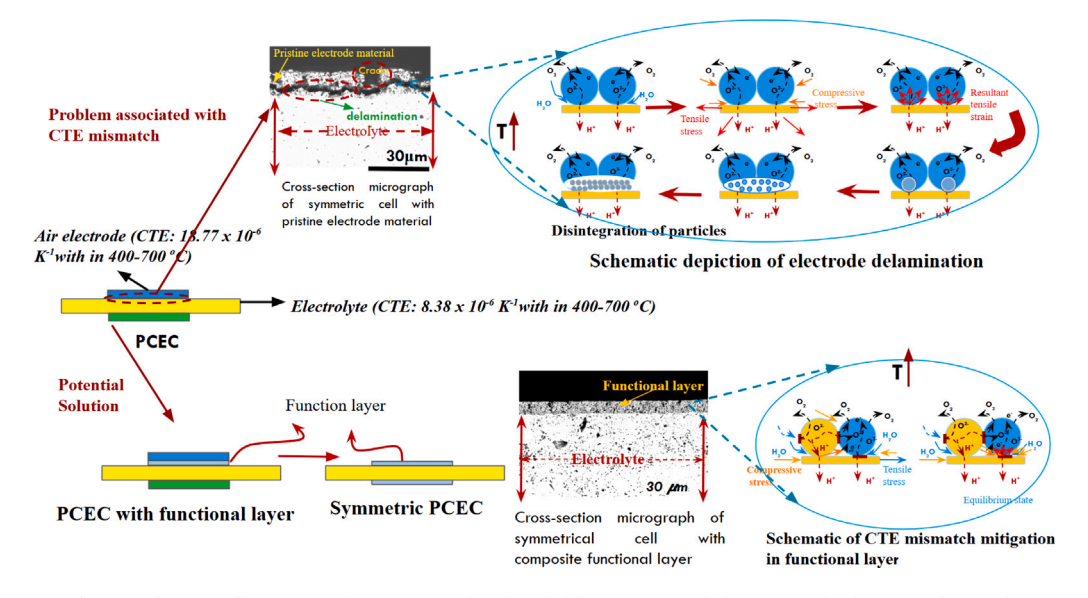


Fig. 1. Schematic illustration of CTE mismatch-induced delamination and the proposed solution in this work.

large-scale  $\rm H_2$  generation, leveraging significant thermodynamic advantages. Operating at elevated temperatures (typically 500–1000 °C) [3, 4], SOE requires considerably less electrical energy, with electrolysis needing only 3.6 kWh of electricity to produce 1 Nm³ of  $\rm H_2$ , compared to 5–6 kWh at room temperature [5]. This high-temperature operation results in a superior electrical efficiency of approximately 74%–81%, compared to the 56%–60% of PEM electrolyzers.

Iwahara et al. [6] further advanced the application of electrolysis for energy storage by introducing proton ceramics for various applications. This led to the development of proton-conducting ceramic electrolysis and fuel cells (PCECs/PCFCs), which are electrochemical devices designed for highly efficient electrical-to-chemical and vice versa energy conversion and storage. A key advantage of PCECs over conventional electrolysis and fuel cells based on oxygen-ion conducting ceramics is their ability to operate at lower to intermediate temperatures (400–700 °C). This lower operating range offers additional benefits, including improved system integration, enhanced fuel utilization, higher purity of produced  $\rm H_2$ , and more effective coupling to various chemical processes.

Furthermore, recent advancements in PCFCs have demonstrated their potential for fuel flexibility and robustness in electricity generation, making them highly durable and tolerant to coking and sulphur [7]. Over the past decade, electrolysis technology based on proton-conducting ceramics has indeed marked significant advancements in materials, components, and cell development [8-13]. Recent comprehensive reviews further underscore these efforts, highlighting the significant progress in materials, components, and cell development, while also reiterating the persistent challenges such as electrode stability and sluggish oxygen evolution reaction kinetics [14]. However, despite this progress, the widespread deployment of PCECs still faces persistent challenges, particularly concerning electrode stability and overall performance. Community efforts are thus dedicated to developing highly performing PCEC steam electrodes with superior contact to the electrolyte [8,9,15-22]. Recent studies by Na Ai et al. [23], who introduced a novel in-situ electrode fabrication method, and Min Xu et al. [24,25], who provided a detailed description of nanoparticle exsolution on electrodes, highlight emerging techniques for advancing solid oxide cell (SOC) preparation and enhancing performance.

 $BaZr_{0.7}Ce_{0.2}Y_{0.1}O_{3-\delta}$  (BZCY721) stands as a state-of-the-art proton conductor, widely employed as a solid electrolyte in PCEC designs. Its composition represents a careful trade-off between thermo-chemical stability, acceptor dopant solubility at elevated temperatures, and the overall performance of Y-substituted  $BaZrO_3$  and  $BaCeO_3$  classes of

materials [6,26-28]. Over the past decade, numerous studies have focused on defining and testing new air/steam electrode materials for PCEC fuel/electrolysis cells. However, many materials initially developed for oxygen-ion conducting cells [29-31] were directly applied in H-SOECs without fully considering the distinct interfacial reactions occurring with proton-conducting electrolytes. The steam electrode reaction mechanism [32] in PCECs is fundamentally distinct from that observed in SOECs/SOFCs, where oxygen ions must also diffuse to the triple-phase boundary (TPB) area. Therefore, an effective steam electrode for PCECs requires good electronic and oxygen-ion conductivities and a robust protonic pathway. To address these requirements and the persistent challenges of sluggish Oxygen Evolution Reaction (OER) kinetics and electrode instability, research on advanced electrode materials for PCECs has focused on various material regulation strategies, including chemical doping, microstructural engineering, and multiphase design [33]. Among promising candidates,  $BaCo_{0.4}Fe_{0.4}Zr_{0.2}O_{3-\delta}$  (BCFZ442) has been widely reported [18,34] as a suitable steam electrode for long-term application. This is attributed to its mixed ionic-electronic conductivity, stable perovskite structure with large Ba2+ cations (facilitating oxygen ion migration), and good catalytic activity stemming from Co/Fe valence state changes [35-40]. For instance, BCFZ442 demonstrates significantly lower polarization resistance compared to La<sub>0.6</sub>Sr<sub>0.4</sub>Co<sub>0.2</sub>Fe<sub>0.8</sub>O<sub>3</sub> (LSCF) (e.g., 8.5 vs. 65  $\Omega cm^2$  at 500 °C), (1.6 vs. 5.1  $\Omega cm^2$  at 600 °C) , further decreasing in humid air (3.9 and 1.0  $\Omega$ cm<sup>2</sup>) at 500 and 600 °C, respectively [18].

One of the key challenges with this material system combination is its poor electrode-electrolyte interface contact during cell processing and operation. Indeed, the electrode-electrolyte interface's mechanical integrity and bonding strength are paramount for long-term cell stability, with studies demonstrating that robust interfaces, where each layer remains flat and firmly attached, contribute significantly to high endurance [7]. As highlighted in our previous research [41], the average coefficient of thermal expansion (CTE) difference between pristing BCFZ442(FL) and BZCY721(EL) samples is approximately 124%. This significant thermal expansion mismatch induces tensile stresses and strains, leading to electrode disintegration, as illustrated in Fig. 1. The resulting interface weakening and fragmentation, as previously reported '[42-44], significantly reduce the density of triple-phase boundaries (TPBs), ultimately degrading the electrode's electrochemical performance. While some approaches focus on ex-situ surface treatments to improve bonding and eliminate delamination, the critical role of interface design and thermal expansion coefficient (TEC) matching for longterm durability has been increasingly recognized. For instance, recent work on  $\text{PrBaMn}_2\text{O}_{5+\delta}$  (PBM) and  $\text{BaZr}_{0.85}\text{Y}_{0.15}\text{O}_{3-\delta}$  (BZY) composite steam electrodes demonstrated exceptional durability over hundreds of hours, attributing this to innovative interface design, including the use of cube-shaped BZY microcrystals for enhanced proton conductivity and a TEC closer to that of the electrolyte [45]. To mitigate this incompatibility-induced degradation, we introduce a novel (to the best of our knowledge) functional composite layer, fabricated with different weight fractions of BCFZ442(FL) and BZCY721(EL) and intended to be positioned between the electrolyte and the air electrode as an intermediate layer. Many researchers have reported on the concept of mixed ionic-electronic conductivity, highlighting that incorporating a second phase can improve the dispersion of active sites for surface water vapor and oxygen, and facilitate interfacial proton transport [9, 15,32,46,47]. The idea of combining two phases in a composite form, a strategy known as multiphase design [33], has been extensively explored in research to improve chemical compatibility, mechanical stability, and electrochemical performance for various applications, such as in PCECs or gas separation membranes [48,49] or gas separation membranes [50-52]. While extensive research has been conducted on BCFZ442 and BZCY721 individually, as well as on various composites in related applications, direct studies focusing on this specific BCFZ442-BZCY721 composite within the context of protonic ceramic electrolysis cells appear to be scarce. Given this lack of existing studies. exploring the combination of BCFZ442 and BZCY721 represents a novel area of research that could provide valuable insights into enhancing the performance and stability of protonic ceramic electrolysis cells. Therefore, our previous and present work focus on advancing research in this area, primarily assessing the compatibility, electrochemical properties, and potential advantages of the BCFZ-BZCY composite as a protonic ceramic electrolysis technology component. As depicted through Fig. 1, this study suggests adding an additional component called a 'functional layer' as an intermediate layer between the electrolyte and the steam electrode to provide a gradual thermal expansion mismatch transition from electrode to electrolyte. To focus this study specifically on the chemical and thermal interaction between the functional layer and electrolyte interface, we have used a symmetrical cell configuration of BCFZ442:BZCY721 || BZZY721+NiO || BCFZ442:BCFZ721. We have limited this study to the functional layer and electrolyte interaction. The integration of this layer within a full cell configuration is in the scope of future investigation.

In our previous work [41], we identified the optimal composition of the composite functional layer along with its fabrication conditions, and demonstrated a reduction in thermal mismatch (see Supplementary Figures 1&2). This study presents an understanding of the electrochemical behavior and microstructure of the interface between the functional layer and electrolyte. In this study, we fabricated symmetrical coin cells where the electrolyte was prepared using cold uniaxial pressing, and the functional layer was applied to the electrolyte using screen printing. Screen printing was chosen for functional layer deposition due to its several advantages, including simplicity, cost-effectiveness, the ability to produce uniform microstructures, and suitability for high-volume production and commercial scalability [53-55]. Typically, a screen printing paste consists of a solid loading material, a dispersant, and a binder solution. Among these components, the binder content significantly influences ink rheology, particle connectivity, mechanical strength, total polarization resistance, and the electrical conductivity of the printed electrode layer/functional layer [56]. Ethyl cellulose (EC) was chosen as the binder because it promotes a uniform and fine microstructure, greater porosity, a homogeneous pore size distribution, and lower polarization resistance [56]. To examine the influence of ethyl cellulose (EC) content on the electrochemical performance and microstructure of the composite functional layer, various EC weight fractions (1 wt%, 3 wt%, and 5 wt%) in the binder solution were studied. Comprehensive electrochemical characterization and microstructural analyses were performed before and after electrochemical impedance spectroscopy (EIS) testing for all symmetrical PCECs within an operating temperature range of 400-700 °C. The findings were compared with those for cells featuring a pristine BCFZ442(FL) electrode and benchmarked against existing literature data.

#### 2. Experimental procedure

#### 2.1. Materials

Steam/air electrode materials: BZCY721(EL) and BCFZ442(FL) were procured from Marion Technologies (France) and CerPoTech (Norway), respectively. The verification of stoichiometry, crystal structure, particle size distribution, and specific surface area of these powders was previously reported [41]. Mixtures of the pristine BaCo $_{0.4}$ Fe $_{0.4}$ Zr $_{0.2}$ O $_{3-\delta}$  (BCFZ442 (FL)) and BaZr $_{0.7}$ Ce $_{0.2}$ Y $_{0.1}$ O $_{3-\delta}$  (BZCY721 (EL)) in ratios of 90:10 (not presented in this article), 70:30 and 50:50 were utilized to prepare the screen printing pastes for deposition of the functional layers.

Solid electrolyte: To achieve adequate sintering of BZCY721(EL) below its typical sintering temperature ( $\geq 1700\,^{\circ}$ C), NiO powder (0.5 wt%) [57] obtained from G. Vogler B.V. (the Netherlands) was incorporated as a sintering aid via ball milling. Using a tumbler mixer, the ball milling process was conducted in a 500 mL polyethylene bottle for 24 h. The average particle size, determined using a Horiba LA-950b V2 particle size analyzer, was 1.99  $\mu m$ . The influence of NiO additive on the sintering behavior of BZCY721(EL) was routinely evaluated using a NETZSCH DIL402C dilatometer with a heating rate of 5 K/min in air at ambient pressure.

#### 2.2. Fabrication of symmetrical PCECs

Disc-shaped BZCY721(EL) electrolyte pellets with a diameter of 25 mm and a thickness of 2 mm were fabricated using a two-step process. First, uniaxial pressing (P/0/Weber) at 100 MPa for 120 s densified the powders into green pellets. Subsequently, cold isostatic pressing (CIP) (EPSI International, Belgium) at 200 MPa for 120 s further enhanced the density. Polyvinyl alcohol (PVA) binder was used to facilitate the pelletization process. The green pellets were then sintered at 1500 °C for 10 h with a heating/cooling rate of 2 K/min in air (refer to Fig. 2) for a flowchart depicting the electrolyte fabrication process. CIP processing resulted in denser pellets than those obtained solely by uniaxial pressing, as evidenced by their darker color. The relative density of the electrolyte (91%) was determined using the Archimedes method with isopropanol (density =  $0.786 \text{ g/cm}^3$  at 20 °C), assuming a theoretical density of 6.20 g/cm<sup>3</sup> for BZCY721(EL). Following the fabrication of high-density electrolyte pellets, symmetrical cells were prepared having the configuration BCFZ442(FL): BZCY721(EL)|BZCY721(EL)+NiO(0.5 wt%)|BCFZ442(FL): BZCY721(EL) (illustrated in Fig. 2). The composite functional layer, with an effective area of 1 cm<sup>2</sup>, was deposited on both sides of the electrolyte using a screen mesh with a wet layer thickness of 40 µm. A two-step screen-printing process was employed to achieve a uniform bilateral coating. After the deposition on one side, the cell was dried at 100 °C in an oven for 15 min before printing the opposite side. After drying, the electrodes were sintered at 1100 °C in air for 5 h [41].

# 2.3. Screen printing paste preparation and optimization

Table 1 details the components used to formulate the screen printing paste. Three primary factors govern the rheology and physical characteristics of the ink: solid loading (powder), dispersion solution, and binder solution. The dispersant preferentially adsorbs onto the particle surface, creating a steric hindrance layer that prevents agglomeration [53]. Conversely, binders, such as ethyl cellulose, enhance the particle network strength within the paste. Studies have shown that the binder content significantly impacts ink rheology, particle connectivity, mechanical strength, and total polarization resistance [53,56]. Therefore, the weight fraction of ethyl cellulose in the binder solution was varied to investigate its influence on these properties. At the same time, other parameters such as sintering temperature and time were kept constant.

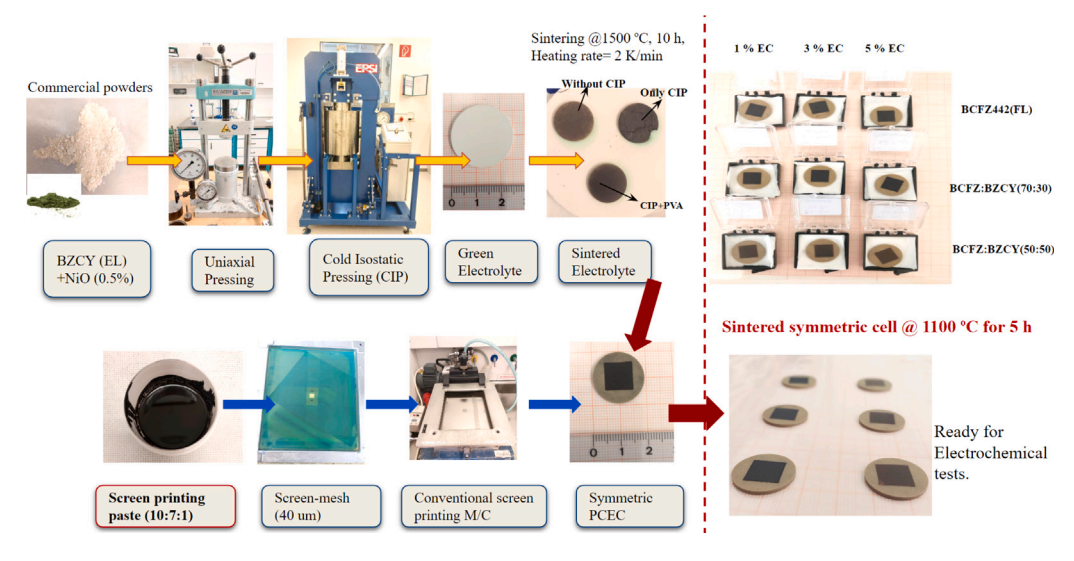


Fig. 2. Flow chart showing the fabrication process for symmetrical PCECs (left), and symmetrical PCECs after sintering at 1100 °C for 5 h (right).

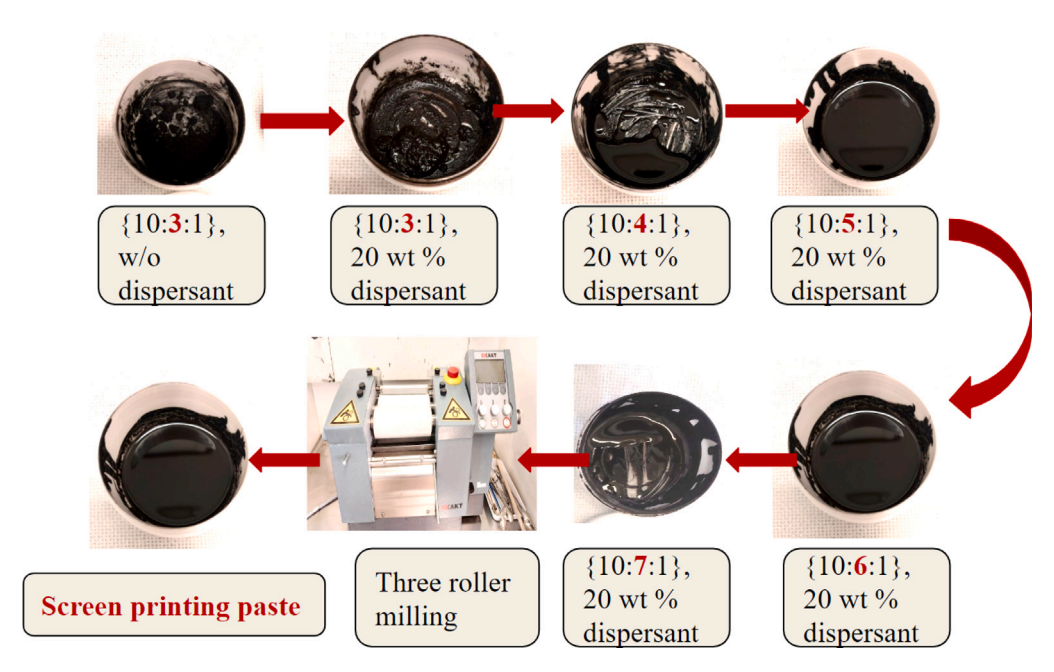


Fig. 3. Process flow for optimizing the screen printing pastes.

**Table 1**Components of screen printing paste.

Ingredients	Used
Solvent	Terpineol (Boiling point: 219 °C)
Binder	Ethyle cellulose (viscosity: 45cP)
Dispersant	BYK-P 104
Solid	BCFZ442(FL)/BZCY721(EL) composites

The preparation of screen printing paste involved a three-step process described in Fig. 3. First, a 20 wt% dispersant solution was mixed with terpineol solvent (80 wt%) [58,59], and a binder solution was formulated by incorporating ethyl cellulose into terpineol at varying weight fractions (1 wt%, 3 wt%, and 5 wt%) using a rotary mixer at 4500 rpm for 5 h. These solutions were then combined with crushed and ground ceramic composite powder to form an initial suspension, which was finally homogenized using a three-roller mill. Building upon a literature-based initial ratio of 10:3:1 (wt%) for powder:dispersant:

binder [58,59], the dispersant solution was adjusted to achieve effective powder dispersion and a visually determined screen-printable viscosity. A three-roller mill was then employed to break down particle agglomerates and homogenize the screen-printing paste using the parameters outlined in Table 2. This optimization process resulted in a final formulation (10:7:1) with a weight ratio of approximately 55% powder loading, 39% dispersant solution, and 6% binder solution.

#### 2.4. Characterization techniques

#### 2.4.1. Electrochemical characterization

To minimize the contribution of current collector resistances, we coated both sides of the PCECs with platinum (Pt) and connected them to Pt mesh current collectors. The symmetrical cells' electrochemical impedance spectroscopy (EIS) was measured using an Alpha-A High Performance Frequency Analyzer (Novocontrol, Montabaur, Germany). The frequency range was swept from 0.1 Hz to 1 MHz with an AC excitation amplitude of 2 mV. Measurements were carried out in a

 Table 2

 Three roller milling parameters of screen printing pastes.

	01 1 01		
Details of pass	Gap between rollers 1 and 2( $\mu m$ )	Gap between rollers 2 and 3 ( $\mu m$ )	RPM
First	70	50	100
Second	50	30	100
Third	30	15	100
Fourth	15	10	100

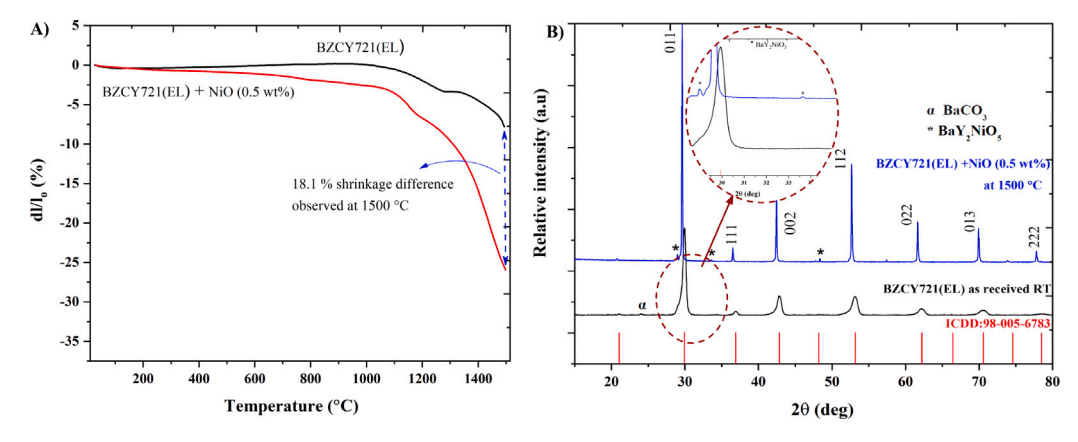


Fig. 4. (A) Linear shrinkage curves for BZCY721(EL) in black and BZCY721(EL) doped with NiO (0.5 wt%) in red; (B) XRD of the BZCY721 pellet (black) and the NiO (0.5 wt%) doped BZCY721(EL) pellet sintered at 1500 °C for 10 h (blue) compared to the ICDD reference peak positions (red). (For interpretation of the references to color in this figure legend, the reader is referred to the web version of this article.)

wet air atmosphere (3 vol.% H<sub>2</sub>O) within a temperature range of 200–700 °C. However, overall cell performance was evaluated in a higher temperature range of 400-600 °C (excluded 700 °C data points due to inconsistencies). The obtained EIS data were analyzed using RelaxIS 3 software (version 3.0.20.19, rhd instruments, Darmstadt, Germany) while Eqs. (1) (2), (3), (4) define the theoretical background.

Since the electrochemical impedance of an electrode reaction depends on the AC frequency (i.e., it has a specific time constant), the distributed relaxation time constant as described in Eq. (2) and the brick layer model were employed to analyze the equivalent circuit, which consisted of a series of parallel resistances and constant phase elements (R||CPE). The capacitance of each R || CPE circuit element was calculated from the corresponding resistance parameter (R), constant phase element (CPE) parameters (Q and  $\alpha$ ) [60–63] using the following equations:

$$C = \frac{Q^{(\frac{1}{\alpha})}}{R^{1-\alpha}} \tag{1}$$

$$\tau = \frac{1}{(\omega)_{max}} = RC \tag{2}$$

$$f = \frac{1}{2\pi RC} \tag{3}$$

$$ASR = \frac{R_p \times A_s}{2} \tag{4}$$

Here, f is the maximum relaxation frequency,  $\tau$  is the time constant,  $R_p$  is the polarization resistance, and  $A_S$  is the effective surface area of 1 mm<sup>2</sup>

### 2.4.2. Microstructural characterization

The microstructures of the samples were investigated using scanning electron microscopy (SEM). Two instruments were employed: a high-resolution field-emission gun SEM (ApreoS, HRSEM) equipped with a backscatter electron (BSE) detector and a tabletop SEM (Hitachi TM3000). Cross-sections were prepared to prepare the samples for SEM analysis. This involved embedding the samples in epoxy resin and curing for 48 h. The embedded samples were then ground and polished progressively finer, with a final polishing step using 50 nm silica nanoparticles (SiO $_2$ ) to achieve a smooth and reflective surface. The

porosity and thickness of the pellets were quantified using ImageJ/Fiji software [64], based on approximately 10 SEM micrographs acquired at different magnifications (30  $\mu$ m, 50  $\mu$ m, and 100  $\mu$ m).

#### 3. Results and discussion

## 3.1. Sintered BZCY721(EL) specimens

This section briefly qualifies the BZCY721(EL) specimens used as electrolyte in manufacturing the symmetrical cells. Although the electrolyte's thermal and structural investigations are mostly routine, they are required to ensure that electrolyte material of sufficient quality, e.g., phase purity and high relative density, is used to deposit the electrode layers. The introduction of NiO (0.5 wt %) significantly alters the sintering behavior of BZCY721(EL) ceramics as demonstrated previously in earlier works [65–67]. Specifically, as shown in Fig. 4A, the onset temperature of sintering shifts by 120 °C (from 1210 °C for BZCY721 to 1090 °C for BZCY721+NiO), and the doped material exhibits 18.1% more linear shrinkage at 1500 °C compared to the pristine material. As described in the section "Fabrication of symmetrical PCECs", a density of above 90% for BZCY721(EL) could only be achieved at T = 1500 °C after combining cold isostatic pressing (CIP) and sintering aid addition. This ensures sufficient mechanical stability of the electrolyte, allowing the electrode layers to be printed onto it. Fig. 4B presents the X-ray diffractograms (Bruker D4 Endeavor, USA, CuKα radiation) of undoped and NiO-doped BZCY721(EL) sintered at 1500 °C for 10 h. The doped BZCY721(EL) XRD reveals that all the main peaks correspond to the perovskite phase. Importantly, adding NiO does not induce any changes in the crystal structure. However, minor peaks at 33.6 ° deviate slightly from the usual reported range (31-33  $^{\circ}$ ) for the BaY<sub>2</sub>NiO<sub>5</sub> phase (ICDD: 00-041-0463) [68, 69]. Additionally, the disappearance of the minor impurity BaCO<sub>3</sub> (Witherite, ICDD: 98-011-0918) peak at 24.082 ° in the doped sintered BZCY721(EL) at higher temperatures suggests enhancing the purity of the perovskite phase. [70]. BaY<sub>2</sub>NiO<sub>5</sub> formation occurs at 900 °C, and due to its relatively low melting temperature (1400-1500 °C), this phase acts as a sintering aid. The color change of the pellet and green traces on the MgO sintering plate suggest Ba evaporation and Ni bulk diffusion, respectively. This is in line with the hypothesis

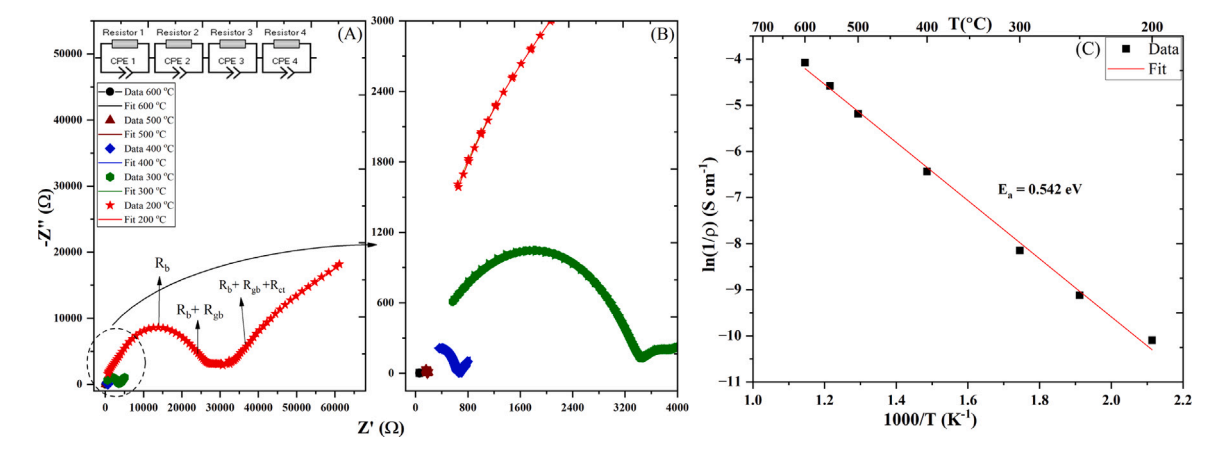


Fig. 5. (A)Nyquist plots of an electrolyte pellet coated with Pt paste, measured at various temperatures in wet air (3 vol. %  $H_2O$ ); (B) Magnified view of the Nyquist plots focusing on the response at 300 °C, 400 °C, 500 °C, and 600 °C; (C) Arrhenius plot of the proton-conducting solid electrolyte BZCY721(EL) + 0.5% NiO.

proposed by Tong et al. [70], who attributed the enhanced sintering kinetics to  ${\rm BaY_2NiO_5}$  decomposition and the subsequent diffusion of Ba, Y, and Ni into BZCY grain boundaries. The routine analysis of phase, structural, and thermal evolution as a function of the selected fabrication technique, i.e., CIP combined with NiO-aided sintering, reveals that the BZCY721(EL) has sufficient quality to be used as a solid electrolyte for the fabrication of the electrodes. Furthermore, introducing the functional layer described in this work is expected to mitigate Ni interdiffusion into the steam electrode.

#### 3.2. Electrochemical analysis by means of EIS

Upon the application of an external voltage during electrolysis, water/steam undergoes dissociation at the triple phase boundary (TPB). This dissociation generates oxygen, protons (H<sup>+</sup>), and electrons. Electrons accumulate near the steam electrode surface, while protons migrate through the bulk proton-conducting solid electrolyte (PCSE), and these combined effects contribute to the formation of the electric double layer (EDL) at the interface. The EDL plays a critical role in the kinetics of electrode-electrolyte interactions, particularly in systems like electrolysis cells. The EDL influences the interface's electric field, affecting the activation energy of charge transfer reactions. The EDL modulates key kinetic parameters such as (i) the exchange current density influenced by the concentration of reactants in the diffuse layer and (ii) the charge transfer resistance affected by the potential drop across the EDL. The EDL's structure can hinder or facilitate ion transport to the reaction site. The structure and thickness of the EDL determine the availability of reactive species at the electrode surface, directly impacting reaction rates. In systems with high current density, the EDL's dynamics can influence ion depletion or accumulation, impacting mass transport.

Designing an effective EDL to facilitate electrochemical reactions requires careful consideration of several key factors. The goal is to optimize ion transport, reduce charge transfer resistance, and enhance reaction kinetics. Amongst the essential factors are the electrode composition, surface properties, and electrolyte composition. In order to achieve a coherent transition from EL material to the steam electrode material, we introduce a ceramic composite functional layer that combines the chemical, electrical, and catalytic properties of the electrolyte and the electrode materials. EDL is frequency-dependent, contributing to capacitive behavior at low frequencies, while kinetic processes dominate at higher frequencies. The formation and dynamics of the EDL have specific time constants and capacitance values. Irvine et al. [62] have suggested a set of capacitance values based on the brick layer model. We calculated these capacitance values using Eqs. (1) and (2) after fitting EIS spectra with an appropriate equivalent circuit using Relaxis.

#### 3.2.1. EIS of electrolyte BZCY721 + NiO(0.5 wt%)

To validate our methodology and fitting parameters for subsequent analysis of symmetrical cells, we conducted an initial EIS study on a bare proton-conducting electrolyte, as detailed in the experimental section, because of the availability of well-established literature for validation. Fig. 5 presents the Nyquist plots of the bare electrolyte coated with Pt paste on both sides. Fig. 5A shows the spectra from 200 °C to 600 °C (please refer to the supplementary material for the detailed EIS pattern). In contrast, Fig. 5B provides a magnified view of the highertemperature spectra. Consistent with previous observations [60,62], increasing temperature resulted in the disappearance of the semicircle corresponding to the bulk impedance and overall spectra shifts towards lower resistances. For the meaningful deconvolution of the EIS, selecting an appropriate equivalent circuit for a given Nyquist plot often involves consideration of two factors: (1) simplicity and (2) alignment with the known physical processes occurring within the system. In this case, relevant processes include bulk grain, grain boundaries, charge transfer, and mass transfer [71]. After evaluating several equivalent circuit models, a combination of four parallel resistor-constant phase element (R||CPE) circuits provided an excellent fit with an acceptable error tolerance within the Relaxis software. Based on the extracted capacitance and relaxation frequency values, the bulk capacitance was estimated to be 10<sup>-12</sup> F, with a maximum relaxation frequency of approximately 10<sup>5</sup> Hz. Fig. 5 A depicts the contribution of each element to the total impedance, where the bulk contribution ends at around 104 Hz, grain boundaries end near 103 Hz, and charge transfer extends down to 4.82 Hz. The low-frequency spike may be attributed to interfacial polarization or proton accumulation at the Pt-electrolyte interface. Fig. 5C depicts the total conductivity of the electrolyte pellet (diameter 19 mm, thickness 1.23 mm) as a function of the inverse temperature. From the slope, activation energy was calculated to be  $0.542 \pm 0.0138$  eV. This value falls within the well-accepted range for proton-conducting electrolytes. A successful validation was done to confirm the efficacy of the chosen equivalent circuits, the analysis methodology, and the fitting parameters for further investigations.

### 3.2.2. EIS of symmetrical PCECs

We employed the same equivalent circuits and fitting parameters established for the bare electrolyte analysis to investigate symmetrical PCECs. Fig. 6 presents the distribution of relaxation time constants (DRT) and the corresponding Nyquist plots for two contrasting cell compositions: pristine BCFZ442(FL) and the composite BCFZ: BZCY(50:50) electrodes. The solid lines in Nyquist Fig. 6 represent the best fit of the experimental data to the proposed circuit model. The goodness of fit was quantitatively assessed by the R<sup>2</sup> (nonlinear) value, which was consistently greater than 0.999 for both composition,

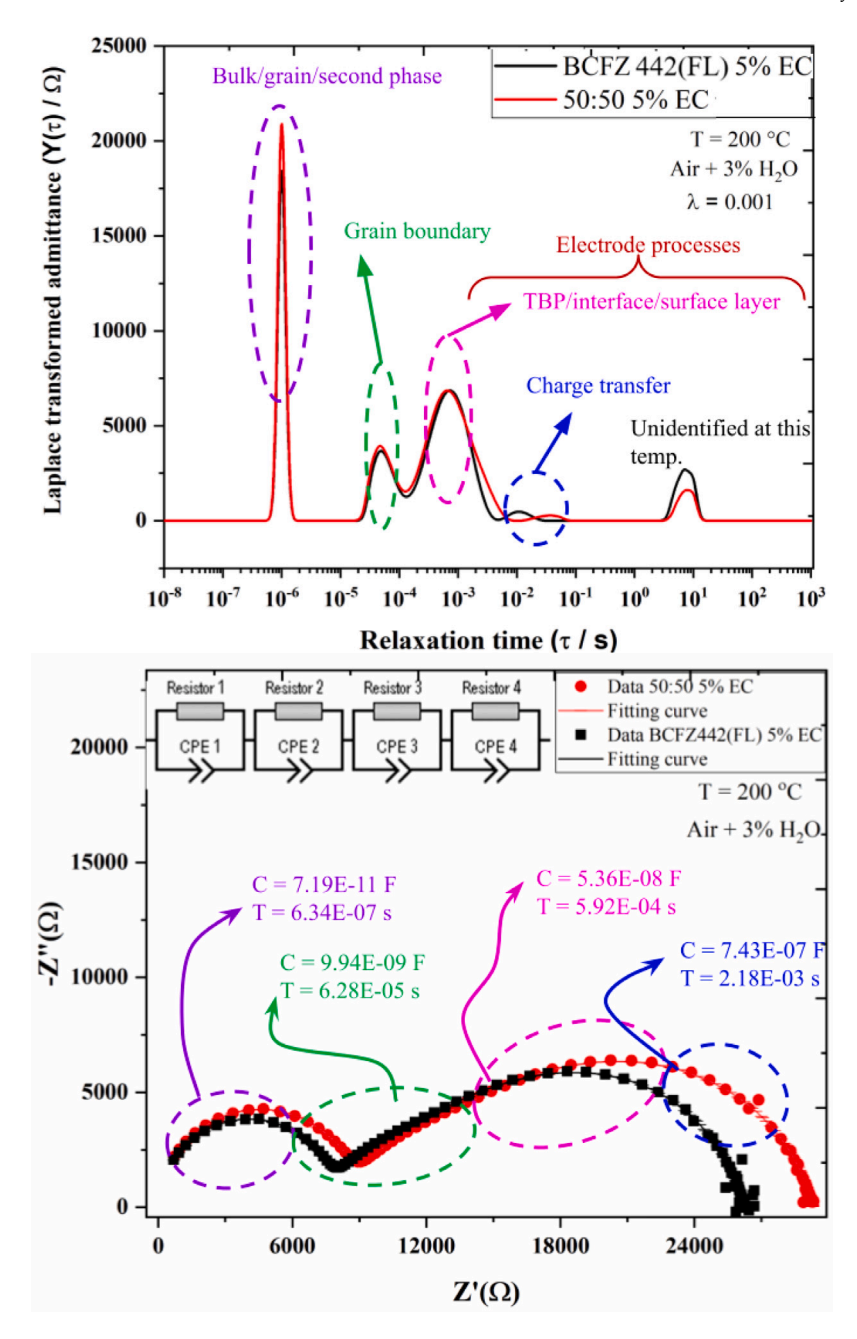


Fig. 6. Complex-plane impedance diagrams (bottom) with the corresponding distribution of relaxation time plots (top) of symmetrical cells fabricated with either pristine BCFZ steam electrodes (black curves) or composite BCFZ: BZCY (50:50) steam electrodes (red curves) measured at 200 °C under the wet air (3 vol. % H2O). Screen-printing pastes were formulated with 5% EC content to fabricate these two types of electrodes. (For interpretation of the references to color in this figure legend, the reader is referred to the web version of this article.)

and the weighted chi-square ( $\chi^2$ ), which was in the order of  $10^4$  (e.g., 104604.11 for BCFZ442(FL)5% EC and 78818.55 for 50:50 5% EC), indicating excellent agreement between the experimental data and the fitted model. We employed the same equivalent circuits and fitting parameters established for the bare electrolyte analysis to investigate symmetrical PCECs.

The DRT plot reveals five distinct peaks, each representing the time constant of a specific electrochemical process. We assigned these phenomena based on the capacitance values and time constants reported in the literature [60,62,72,73]. The peaks in the DRT plots (Fig. 6, top) were attributed to grain bulk (interior): capacitance (C) = 7.19 x  $10^{-11}$  F, time constant ( $\tau$ ) = 6.34  $\times$   $10^{-7}$  s, grain boundaries: C = 9.94  $\times$   $10^{-9}$  F,  $\tau$  = 6.28  $\times$   $10^{-5}$  s. The time constant range- of  $10^{-3}$  - 10 s likely represents processes related to the air electrode, such as those occurring

at the triple phase boundary (TPB) or the electrode electrolyte interface (C =  $5.36 \times 10^{-8}$  F), including charge transfer (C =  $7.43 \times 10^{-7}$  F). An unidentified peak appears in the DRT plot within the time scale of 1 to 10 s at 200 °C. However, at substantially higher temperatures ( $\geq 400$  °C), this peak could be associated with gas phase diffusion/transport through porous electrode [62] (C  $\approx 10^{-2}$  F,  $\tau \approx 1$ –10 s) or other high-temperature electrochemical reactions occurring at the electrode.

Fig. 7 explores the influence of the temperature and the binder content on the impedance response of symmetrical PCECs. Fig. 7(A) presents Nyquist plots for all investigated compositions and binder contents at 400 °C. Fig. 7(B) focuses on the cells with BCFZ: BZCY (70:30) steam electrode fabricated with various binder content, showcasing the impedance spectra recorded in the temperature range of 400 °C to 600 °C. Fig. 7(C) depicts a magnified view of the same composition as

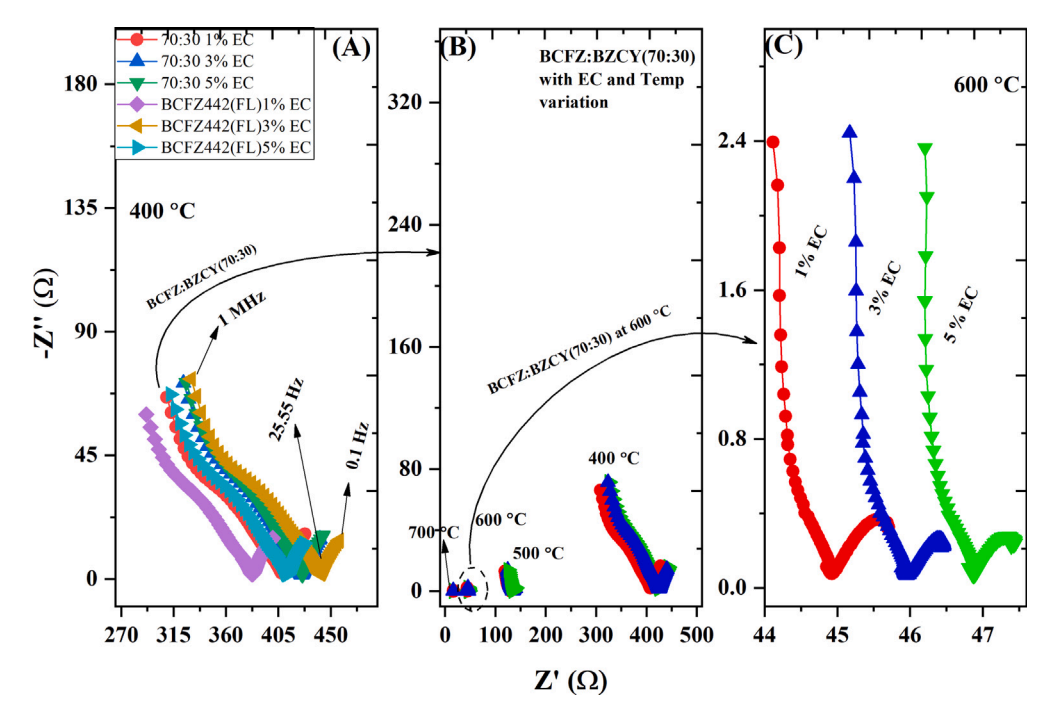


Fig. 7. Nyquist plots of A) Symmetrical cells at 400 °C; B) BCFZ: BZCY(70:30) with various EC contents at elevated temperature in the range 400–600 °C, with C) magnified view at 600 °C showing clearly the effect of the binder used (solid lines connect data points for comparison purposes).

Table 3

The ASR and corresponding activation energy of the electrode in different symmetrical cell configurations at 600 °C in air.

Electrode	Electrolyte	ASR (Ωcm²)	Ea (eV)	Ref
BaCo <sub>0.4</sub> Fe <sub>0.4</sub> Zr <sub>0.2</sub> O <sub>3-<math>\delta</math></sub>	$BaCe_{0.7}Y_{0.1}Zr_{0.1}Yb_{0.1}O_{3\delta} + NiO (1 wt\%)$	1	0.78	[35]
$BaCo_{0.4}Fe_{0.4}Zr_{0.2}O_{3-\delta}$	$BaCe_{0.7}Y_{0.1}Zr_{0.1}Yb_{0.1}O_{3-\delta}$	1.62	1.02	[74]
$Ba_{0.5}Sr_{0.5}Co_{0.8}Fe_{0.2}O_{3-\delta}$	$BaCe_{0.7}Y_{0.1}Zr_{0.1}Yb_{0.1}O_{3-\delta}$	1.77	0.98	[74]
$BaCo_{0.4}Fe_{0.4}Zr_{0.2}O_{3-\delta}$	$BaCe_{0.7}Y_{0.1}Zr_{0.1}Yb_{0.1}O_{3-\delta}$	10	1.22	[48]
$BaCo_{0.4}Fe_{0.4}Zr_{0.1}Y_{0.1}O_{3-\delta}$	$BaCe_{0.7}Y_{0.1}Zr_{0.1}Yb_{0.1}O_{3-\delta}$	4.5	0.92	[48]
$BaCo_{0.4}Fe_{0.4}Zr_{0.2}O_{3-\delta}$	$BaCe_{0.2}Y_{0.1}Zr_{0.7}O_{3-\delta} + NiO (0.5 wt\%)$	1.35	0.87	This work
(70 wt%) $BaCo_{0.4}Fe_{0.4}Zr_{0.2}O_{3-\delta}/(30$ wt%) $BaZr_{0.7}Ce_{0.2}Y_{0.1}O_{3-\delta}$	$BaZr_{0.7}Ce_{0.2}Y_{0.1}O_{3-\delta} + NiO (0.5 wt\%)$	0.99	0.94	This work

in B) recorded at 600 °C. As the temperature increases, the semicircles corresponding to the bulk and grain boundary contributions gradually diminish, indicating increased bulk and grain boundary conductivity. Furthermore, features associated with the electrode activity become more prominent in the Nyquist plots. A low-frequency spike inclined at 45 ° starts appearing between 300 °C and 350 °C, attributed to the gaseous diffusion of oxygen molecules or solid-state diffusion of oxygen ions through the porous electrode [62]. At temperatures exceeding 500-550 °C, the inclined spike transitions into a distinct semicircle, suggesting limited oxygen diffusion by a layer of finite thickness at higher temperatures (Fig. 7 C). This fact leads to the conclusion that below 300 °C, a notable charge transfer is observed at the PCEC interface, while above 550 °C, diffusion processes are contributing more than the transfer of charges to the overall electrode response. Above 600 °C, the electrode behavior shifts towards a capacitive response.

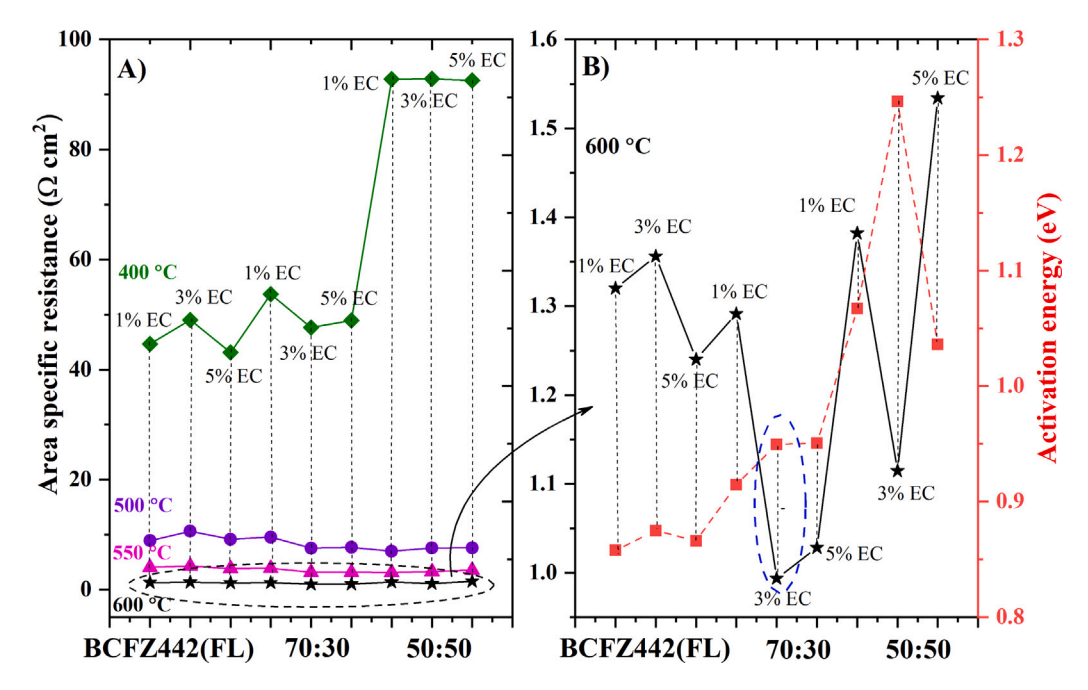
# 3.3. EIS and microstructural analysis of functional layer

Fig. 8 presents a comprehensive analysis of the area-specific resistance (ASR) for various symmetrical PCECs in a range of operating temperatures, i.e., 400–600 °C. Fig. 8(A) depicts the overall trend. In contrast, Fig. 8(B) provides a zoomed-in view of the ASR and corresponding activation energy of symmetrical cells evaluated at 600 °C. This temperature is selected as a typical operational value, for which data are also provided in the referenced literature sources. The ASR behavior of BCFZ: BZCY (50:50) with 3% EC exhibits a distinct anomaly at 400 °C (Fig. 8 A), where its ASR undergoes a sharp transition from

the highest value at 400 °C to the lowest at 600 °C. This behavior can be attributed to the activation of proton conduction. At temperatures below or around 400 °C, proton mobility in BZCY721 may be limited due to insufficient thermal energy to overcome the activation energy for proton transport. Between 400 °C and 600 °C, proton conduction becomes thermally activated, significantly improving ionic conductivity and reducing ASR. In contrast, pristine BCFZ442(FL) with 3% EC exhibits the highest ASR within the investigated temperature range. Interestingly, BCFZ: BZCY (70:30) with 3% binder demonstrates the most favorable performance, achieving a minimum ASR of 0.99  $\Omega$  cm² with an activation energy of 0.94 eV. This value aligns well with previously reported data for air/steam electrodes under similar conditions (Table 3).

High-resolution scanning electron microscopy (HR-SEM) along with energy-dispersive X-ray spectroscopy (EDX) (Fig. 9) was employed to examine the microstructure of BCFZ: BZCY composites (70:30 and 50:50 weight ratios) before and after electrochemical impedance spectroscopy (EIS) testing. The SEM images show that the electrode/electrolyte interface remains intact in all samples, with no visible signs of delamination, cracking, warping, or other interfacial disruption. This confirms excellent structural integrity, with a continuous and well-bonded interface in the 70:30 and 50:50 composites.

Consistently, EDX maps reveal that all expected elements are present near the interface in approximately their nominal proportions. The elemental distribution appears uniform across both sides of the junction, consistent with the intended composite formulation. Minor interdiffusion of Co and Fe into the electrolyte is observed, more prominently



**Fig. 8.** (A) ASR variation (Y-axis) of the symmetrical cells (X-axis) fabricated with pristine or composite electrodes containing various amounts of ethyl cellulose depicted in the 400–600 °C (the colored legends represent temperature, and the data points should correspond to the horizontal axis B) Magnified view of the ASR of all cells at 600 °C with the corresponding activation energies (plotted in red), (data points are connected by solid lines for comparison purposes). (For interpretation of the references to color in this figure legend, the reader is referred to the web version of this article.)

**Table 4**Summary of the thickness of the functional layer measured at the center of the symmetrical cells.

Compositions	Thickness(µm)	ASR (Ωcm²) at 600 °C
BCFZ442(FL) 1%EC	10 ± 0.77	1.32
BCFZ442(FL) 3%EC	$7 \pm 0.78$	1.35
BCFZ442(FL) 5%EC	$25 \pm 1.41$	1.24
BCFZ:BZCY(70:30) 1%EC	$14 \pm 0.71$	1.29
BCFZ:BZCY(70:30) 3%EC	$10 \pm 0.56$	0.99
BCFZ:BZCY(70:30) 5%EC	$15 \pm 0.91$	1.02
BCFZ:BZCY(50:50) 1%EC	$25 \pm 0.68$	1.38
BCFZ:BZCY(50:50) 3%EC	$22 \pm 0.99$	1.11
BCFZ:BZCY(50:50) 5%EC	$33\pm0.98$	1.53

in the 50:50 composition, likely due to the higher sintering temperature. Overlay maps confirm that each element spans its respective phase without significant segregation or depletion, indicating adequate powder mixing and sintering.

In the 70:30 composite, small Ni-rich particulates are observed to cluster near the interface, while no Ni signal is detected elsewhere. This localized agglomeration is likely a processing artifact, as NiO was used as a sintering aid for BZCY721(EL). The incomplete dissolution of Ni during sintering may have led to localized clustering; however, these particles are unlikely to impact the overall electrode performance.

Fig. 10 presents a collection of SEM images that elucidate the influence of both composition (horizontal axis) and ethyl cellulose (EC) content in the binder solution (vertical axis) on the electrode layer microstructure. It is important to note that all microstructures were captured in and around the cells' center to ensure comparison consistency. The average porosity of the BCFZ: BZCY 70:30 and BCFZ: BZCY 50:50 composite functional layer was approximately determined to be 36.37% (standard deviation 5.96%) and 32.32% (standard deviation 6.10%), respectively. Notably, some cells depicted here underwent EIS testing beforehand and possess an additional Pt paste layer for comparison purposes.

The micrographs reveal that pristine BCFZ442(FL) exhibits visible cracking, unlike the BCFZ: BZCY (70:30 and 50:50) composites, which

remain crack-free regardless of binder content. Notably, the functional layers deposited via screen printing show a non-monotonic trend in both thickness and area-specific resistance (ASR) with increasing ethyl cellulose (EC) content, as summarized in Table 4. For both composite formulations, the minimum values of thickness and ASR are observed at 3% EC. As previously established, binder content plays a critical role in governing ink rheology, particle connectivity, and the strength of the resulting particle network. The optimum binder content improves the interconnection between metal–metal and metal-oxide particles by strengthening the particle network within the ink. Particle bridging occurs via hydrogen bonding between the hydroxyl groups of the macromolecular chain in the ethyl cellulose binder and oxygen on the surface of oxide particles, leading to flocculation. Consequently, the degree of flocculation and network strength depends on the EC content and the availability of surface oxygen to form hydrogen bonds [75].

We hypothesize that the initial reduction in ASR and thickness with increasing EC content arises from an optimal balance between binder concentration and surface oxygen availability, promoting effective flocculation and denser particle packing. However, beyond 3% EC, the surface oxygen may become insufficient to interact with all hydroxyl groups. In this case, excess hydrogen bonding interactions may occur between already bonded sites, potentially disturbing the floc structure and weakening particle bridging and network integrity. This, in turn, would lead to a consecutive rise in both layer thickness and ASR. In contrast, for pristine BCFZ442(FL), although the minimum thickness is also observed at 3% EC, this coincides with the highest ASR. This discrepancy may result from a poorly developed particle network with insufficient triple-phase boundaries (TPBs) and limited electrochemically active surface area. Furthermore, incorporating BZCY721(EL) into the composite may enhance TPB density and influence ASR and thickness, depending on the interplay between binder content, BZCY721(EL) loading, and operational temperature.

BCFZ: BZCY (70:30) exhibits the lowest ASR at 3% EC across the operational temperature range among the investigated compositions. The enhanced performance of the 70:30 composition can be attributed to a synergistic combination of factors:

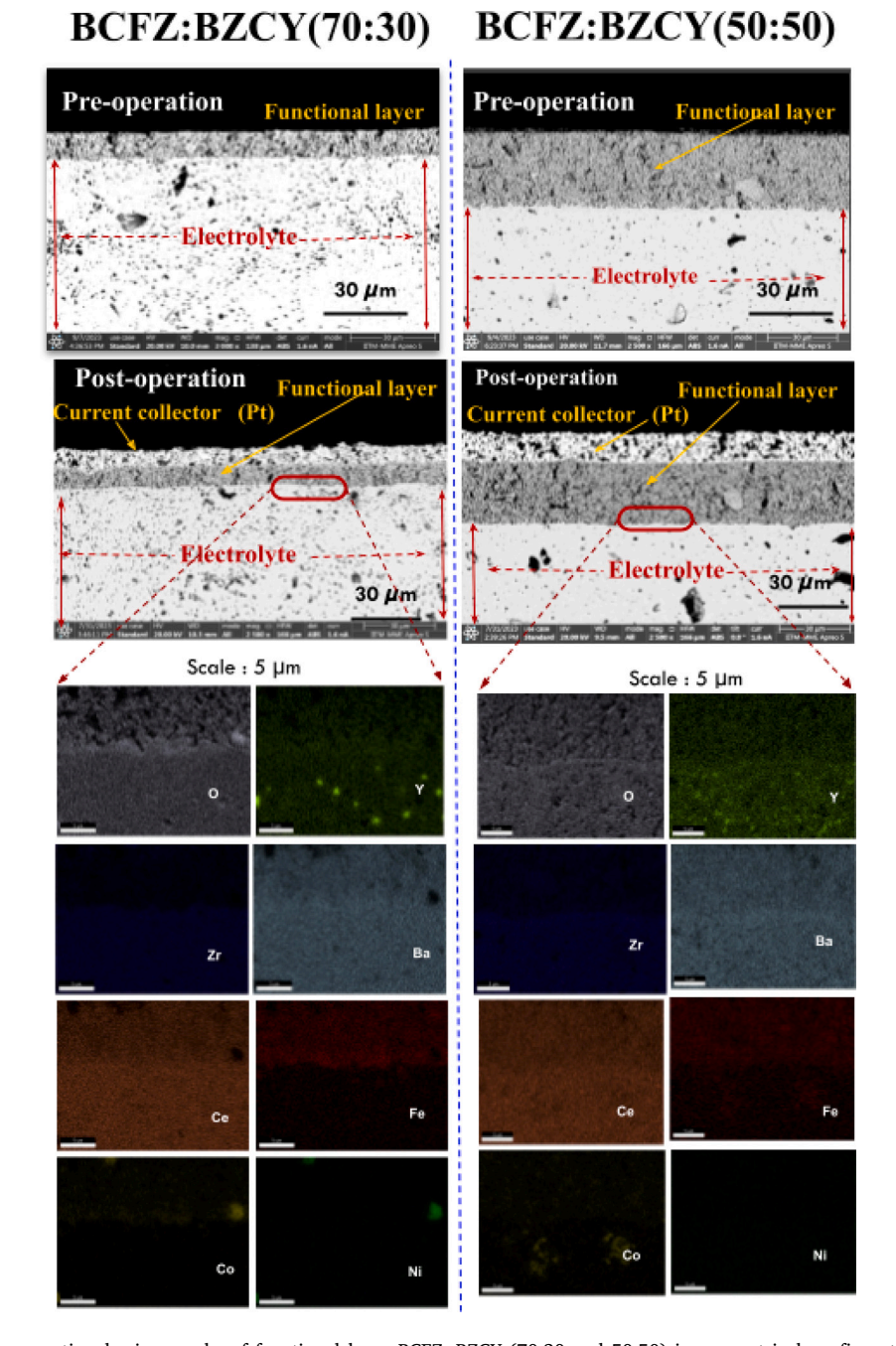


Fig. 9. Comparative SEM cross-sectional micrographs of functional layer BCFZ: BZCY (70:30 and 50:50) in symmetrical configuration, shown before and after EIS testing, and corresponding EDX analysis.

- i. We hypothesize that incorporating the secondary phase BZCY721(EL) effectively balances the oxygen vacancy concentration, optimizing both ionic and electronic conductivity. As reported by Ji et al. [76], oxygen vacancies significantly influence the electronic structure, crystal structure, and surface chemistry of perovskite oxides. XRD analysis from our previous study [41] confirmed that the crystal structure remained unchanged, indicating that the observed effects are primarily due to modifications in the electronic structure. These alterations promote the formation of electron holes and redox couples, enhancing charge transfer and the oxygen evolution reaction. However, an excessive concentration of oxygen vacancies could disrupt the formation of these electron holes and redox couples, potentially hindering charge transport. The 30 wt% fraction of BZCY721(EL) achieves an optimal balance of oxygen vacancy
- concentration. Furthermore, incorporating BZCY721(EL) may reduce the loss of lattice oxygen in BCFZ442(FL), thereby increasing electrostatic attraction within the composite. This reduction mitigates CTE inflection and mismatch with the electrolyte, ultimately improving chemical compatibility.
- ii. As demonstrated in a previous study [41], sintering at 1100 °C induces slight interdiffusion of elements such as Co and Fe, which thermally activates BZCY721(EL) by lowering its sintering temperature and thereby facilitating proton hopping.
- iii. The dual-phase microstructure of the functional layer enhances the reactive surface area by increasing triple-phase boundaries (TPBs) while maintaining the required porosity [53] of approximately 36%. This structure also facilitates effective percolation pathways for gas diffusion. At 3% EC, the binder content appears optimal, improving rheological properties and screen-printing

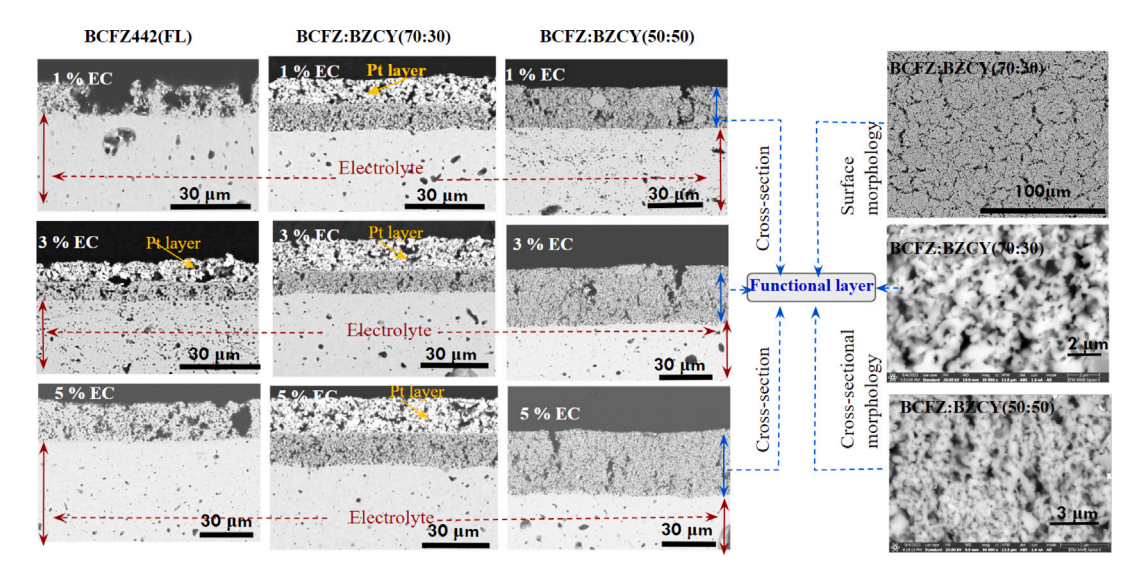


Fig. 10. Cross-sectional SEM micrographs depicting symmetrical cells with variations in ethyl cellulose content (vertical axis) and electrode composition (horizontal axis), showcasing surface morphology and percolation networks of BCFZ: BZCY (70:30) (the right panel of the figure).

quality and promoting a robust particle network. As discussed earlier, hydrogen bonding between hydroxyl groups in the ethyl cellulose binder and surface oxygen on oxide particles fosters flocculation, which enhances particle bridging and packing. This improved connectivity among metallic and oxide phases increases the density of active TPBs and helps minimize ASR, in agreement with previous findings [56,75,77,78].

Moreover, the electrochemical performance of BCFZ: BZCY (70:30) confirms that incorporating a functional layer will not hinder steam electrode operation and electrochemical activity. Instead, it will gradually transition from the steam electrode to the solid electrolyte, consequently mitigating delamination and crack formation. These findings also emphasize the crucial role of a well-structured microarchitecture and a percolating network in achieving high-performance electrodes. The precise combination of constituent materials, their weight ratios, and binder content is essential for optimizing the microstructure and facilitating efficient electrochemical processes.

While experimental stability testing (please refer to Supplementary Figures 3&4 for chemical stability) of the specific symmetrical cell configuration (BCFZ442/BZCY721|BZCY721|BCFZ442/BZCY721) is beyond the scope of this work, insights can be drawn from existing literature on similar compositions and configurations. Reported values for the area-specific resistance (ASR) of materials with a composition similar to BCFZ442 range from 0.075 to 1.4  $\Omega$  cm $^{-2}$ , with an average of 0.73  $\Omega$  cm $^{-2}$  at 600 °C [35,79,80]. Under wet air conditions, the ASR remains stable for approximately 180 h. Based on these literature values, the proposed functional layer in full cell configuration is expected to demonstrate reasonable stability under electrolysis conditions. Future work from our group, which is in process, will validate these findings.

#### 4. Conclusions

This study introduced the concept of incorporating an additional component — a functional layer — into a proton-conducting electrolysis cell and investigated its interaction with the solid electrolyte. We systematically examined the impact of adding a proton-conducting electrolyte material to the steam electrode material, varying their weight fractions and binder content within the screen-printing paste. This allowed us to assess the developed functional layer's electrochemical performance (Area-Specific Resistance, ASR).

A screen-printing paste formulation was successfully optimized, consisting of 55% solid loading, 39% dispersant solution, and 6%

binder solution. This formulation proved suitable for fabricating the functional layer and demonstrated potential applicability in steam electrode processing. Using this optimized composition, a low ASR of 0.99  $\Omega\,\text{cm}^2$  and a favorable activation energy of 0.94 eV were achieved for the BCFZ: BZCY (70:30) material with 3 wt% ethyl cellulose.

The enhanced performance observed is attributed to the synergistic effects of increased triple-phase boundaries (TPBs) and an optimized concentration of oxygen vacancies. These improvements were facilitated by the controlled addition of BZCY721(EL), which boosted both ionic and electronic conductivity. Furthermore, the optimized binder content promoted a well-connected particle network, leading to a thinner functional layer and reduced polarization resistance. Crucially, the functional layer effectively mitigates issues such as delamination and cracking while ensuring strong adhesion and a coherent compositional transition at the interface. Rather than compromising the performance, the functional layer can enhance the electrochemical characteristics of the electrode and is, therefore, expected to improve the cell's overall performance.

# CRediT authorship contribution statement

Shivam Kumar Dwivedi: Writing – review & editing, Writing – original draft, Visualization, Methodology, Investigation, Formal analysis, Data curation, Conceptualization. Yuan Zeng: Writing – review & editing, Methodology, Investigation, Formal analysis. Laura-Alena Schaefer: Writing – review & editing, Methodology. Muhammad Shirjeel Khan: Writing – review & editing, Supervision. Kwati Leonard: Writing – review & editing, Supervision. Norbert H. Menzler: Writing – review & editing, Supervision, Resources, Funding acquisition. Olivier Guillon: Writing – review & editing, Supervision, Resources, Funding acquisition. Mariya E. Ivanova: Writing – review & editing, Validation, Supervision, Resources, Project administration, Funding acquisition, Conceptualization. Ravi Kumar: Writing – review & editing, Supervision, Resources, Funding acquisition, Conceptualization.

# **Declaration of competing interest**

The authors declare that they have no known competing financial interests or personal relationships that could have appeared to influence the work reported in this paper.

#### Acknowledgments

We gratefully acknowledge the Junior Research Fellowship from IIT Madras- RWTH Aachen University and the Indo-German Center for Sustainability graduate research grant. The Helmholtz Association of German Research Centers (HGF) and the Federal Ministry of Education and Research, Germany (BMBF), Germany are gratefully acknowledged for supporting the development of H<sub>2</sub> generation technologies within the frame of the Innovation Pool project "Solar H<sub>2</sub>: Highly Pure and Compressed" and the Helmholtz Research Program "Materials and Technologies for the Energy Transition" (MTET). The German Research Foundation (Deutsche Forschungsgemeinschaft DFG) also funds the publication - 491111487. Open Access funding is enabled and organized by the project DEAL. We also thank Christian Lenser from IMD-2, Forschungszentrum Jüelich GmbH, and the colleagues from the Laboratory for High-Performance Ceramics, IIT Madras, for their support and technical discussion.

Mariya E. Ivanova acknowledges the support of the Bulgarian Ministry of Education and Science through the Bulgarian National Recovery and Resilience Plan, Component "Innovative Bulgaria", project No BG-RRP-2.004-0006-C02, titled "Development of research and innovation at Trakia University in service of health and sustainable well-being."

#### Appendix A. Supplementary data

Supplementary material related to this article can be found online at https://doi.org/10.1016/j.ijhydene.2025.151426.

#### References

- [1] Zhang X, Wang J, Habudula G, Liu J, Kang T. A review of gas-liquid flow characteristics of anode porous transport layer in proton exchange membrane electrolysis cell. Int J Hydrog Energy 2025;100:1010-29.
- [2] Qiao F. Photoelectrocatalytic hydrogen production: Hydrogen production principle, performance optimization strategy, application and prospect. Nano Res Energy 2025;4(1).
- [3] Lu B, Zhang Z, Zhang Z, Zhang C, Zhu L, Huang Z. Control strategy of solid oxide electrolysis cell operating temperature under real fluctuating renewable power. Energy Convers Manage 2024;299:117852.
- [4] Elder R, Cumming D, Mogensen MB. High temperature electrolysis. In: Carbon dioxide utilisation. Elsevier; 2015, p. 183–209.
- [5] Ursua A, Gandia LM, Sanchis P. Hydrogen production from water electrolysis: current status and future trends. Proc IEEE 2011;100(2):410–26.
- [6] Iwahara H, Esaka T, Uchida H, Maeda N. Proton conduction in sintered oxides and its application to steam electrolysis for hydrogen production. Solid State Ion 1981;3–4:359–63. http://dx.doi.org/10.1016/0167-2738(81)90113-2, URL https://www.sciencedirect.com/science/article/pii/0167273881901132.
- [7] Duan C, Kee RJ, Zhu H, Karakaya C, Chen Y, Ricote S, et al. Highly durable, coking and sulfur tolerant, fuel-flexible protonic ceramic fuel cells. Nature 2018;557(7704):217–22.
- [8] Ivanova ME, Peters R, Müller M, Haas S, Seidler MF, Mutschke G, et al. Technological pathways to produce compressed and highly pure hydrogen from solar power. Angew Chem Int Ed 2023;62(32):e202218850.
- [9] Wang Q, Ricote S, Chen M. Oxygen electrodes for protonic ceramic cells. Electrochim Acta 2023;446:142101.
- [10] Zeng Y, Kindelmann M, Leonard K, Schäfer L-A, Yao K, Malzbender J, et al. Characterization of high Zr/Ce ratio Ba (Zr, Ce, Y) O 3-  $\delta$  proton conductors: investigating the impact of y on the properties of materials. Phys Chem Chem Phys 2025;27(2):885–96.
- [11] Leonard K, Okuyama Y, Ivanova ME, Meulenberg WA, Matsumoto H. Tailored and improved protonic conductivity through Ba (ZxCe10- x) 0.08 Y0. 2o3- δ ceramics perovskites type oxides for electrochemical devices. ChemElectroChem 2022;9(4):e202101663.
- [12] Leonard K, Deibert W, Ivanova ME, Meulenberg WA, Ishihara T, Matsumoto H. Processing ceramic proton conductor membranes for use in steam electrolysis. Membranes 2020;10(11):339.
- [13] Deibert W, Ivanova ME, Huang Y, Merkle R, Maier J, Meulenberg WA. Fabrication of multi-layered structures for proton conducting ceramic cells. J Mater Chem A 2022;10(5):2362–73.
- [14] Wang J, Chen W, Wang Y, Wei J, Zhang W, Sun C, et al. Recent advances in proton-conducting solid oxide electrolysis cells. Mater Sci Eng. B 2025;317:118188.
- [15] Bi L, Boulfrad S, Traversa E. Steam electrolysis by solid oxide electrolysis cells (SOECs) with proton-conducting oxides. Chem Soc Rev 2014;43(24):8255–70.

- [16] Lei L, Zhang J, Yuan Z, Liu J, Ni M, Chen F. Progress report on proton conducting solid oxide electrolysis cells. Adv Funct Mater 2019;29(37):1903805.
- [17] Nechache A, Hody S. Alternative and innovative solid oxide electrolysis cell materials: A short review. Renew Sustain Energy Rev 2021;149:111322.
- [18] Tarutina LR, Gordeeva MA, Matkin DE, Akopian MT, Starostin GN, Kasyanova AV, et al. Why do BaCo<sub>0.4</sub>Fe<sub>0.4</sub>Zr<sub>0.1</sub>Y<sub>0.1</sub>O<sub>3-δ</sub>-derived complex oxides become one of the most promising electrodes for protonic ceramic electrochemical cells? An explanatory review. Chem Eng J 2024;151615.
- [19] Téllez Lozano H, Druce J, Cooper SJ, Kilner JA. Double perovskite cathodes for proton-conducting ceramic fuel cells: are they triple mixed ionic electronic conductors? Sci Technol Adv Mater 2017;18(1):977–86.
- [20] Poetzsch D, Merkle R, Maier J. Proton conductivity in mixed-conducting BSFZ perovskite from thermogravimetric relaxation. Phys Chem Chem Phys 2014;16(31):16446–53.
- [21] Strandbakke R, Cherepanov VA, Zuev AY, Tsvetkov DS, Argirusis C, Sourkouni G, et al. Gd-and pr-based double perovskite cobaltites as oxygen electrodes for proton ceramic fuel cells and electrolyser cells. Solid State Ion 2015;278:120–32.
- [22] Vøllestad E, Strandbakke R, Tarach M, Catalán-Martínez D, Fontaine M-L, Beeaff D, et al. Mixed proton and electron conducting double perovskite anodes for stable and efficient tubular proton ceramic electrolysers. Nat Mater 2019;18(7):752–9.
- [23] Ai N, Zou Y, Chen Z, Chen K, et al. Progress on direct assembly approach for in situ fabrication of electrodes of reversible solid oxide cells. Mater Rep: Energy 2021;1(2):100023.
- [24] Xu M, Cao R, Qin H, Zhang N, Yan W, Liu L, et al. Exsolved materials for CO2 reduction in high-temperature electrolysis cells. Mater Rep: Energy 2023;3(2):100198.
- [25] Ni C, Zhou J, Zhang Z, Li S, Ni J, Wu K, et al. Iron-based electrode materials for solid oxide fuel cells and electrolysers. Energy & Environ Sci 2021:14(12):6287–319.
- [26] Kreuer K. Proton-conducting oxides. Annu Rev Mater Res 2003;33(1):333–59. http://dx.doi.org/10.1146/annurev.matsci.33.022802.091825.
- [27] Schober T, Bohn H. Water vapor solubility and electrochemical characterization of the high temperature proton conductor BaZr<sub>0.9</sub>Y<sub>0.1</sub>O<sub>2.95</sub>. Solid State Ion 2000;127(3–4):351–60.
- [28] Ricote S, Bonanos N, Caboche G. Water vapour solubility and conductivity study of the proton conductor  $BaCe_{0.9-x}Zr_xY_{0.1}O_{3-\delta}$ . Solid State Ion 2009;180(14–16):990–7.
- [29] Zhou W, Shao Z, Ran R, Zeng P, Gu H, Jin W, et al. Ba<sub>0.5</sub>Sr<sub>0.5</sub>Co<sub>0.8</sub>Fe<sub>0.2</sub>O<sub>3-δ</sub>+ LaCoO<sub>3</sub> composite cathode for Sm<sub>0.2</sub>Ce<sub>0.8</sub>O<sub>1.9</sub>-electrolyte based intermediatetemperature solid-oxide fuel cells. J Power Sources 2007;168(2):330–7.
- [30] Zhou W, Shao Z, Ran R, Gu H, Jin W, Xu N. LSCF nanopowder from cellulose–glycine-nitrate process and its application in intermediate-temperature solid-oxide fuel cells. J Am Ceram Soc 2008;91(4):1155–62.
- [31] Zhang W, Yu B, Xu J. Investigation of single SOEC with BSCF anode and SDC barrier layer. Int J Hydrog Energy 2012;37(1):837–42.
- [32] He F, Song D, Peng R, Meng G, Yang S. Electrode performance and analysis of reversible solid oxide fuel cells with proton conducting electrolyte of BaCe<sub>0.5</sub>Zr<sub>0.3</sub>Y<sub>0.2</sub>O<sub>3...δ</sub>. J Power Sources 2010;195(11):3359–64.
- [33] Liu Z, Zhang L, Zheng CJ, Zhang Y, Chen B, Shao Z, et al. Advanced electrode materials for efficient hydrogen production in protonic ceramic electrolysis cells. Adv Mater 2025;2503609.
- [34] Kasyanova AV, Tarutina LR, Rudenko AO, Lyagaeva JG, Medvedev DA. Ba (Ce, Zr) O<sub>3</sub>-based electrodes for protonic ceramic electrochemical cells: towards highly compatible functionality and triple-conducting behaviour. Russ Chem Rev 2020;89(6):667.
- [35] Shang M, Tong J, O'Hayre R. A promising cathode for intermediate temperature protonic ceramic fuel cells: BaCo<sub>0.4</sub>Fe<sub>0.4</sub>Zr<sub>0.2</sub>O<sub>3-δ</sub>. RSC Adv 2013;3:15769–75. http://dx.doi.org/10.1039/C3RA41828F.
- [36] Yang L, Gu X, Tan L, Zhang L, Wang C, Xu N. Role of  $ZrO_2$  addition on oxygen transport and stability of  $ZrO_2$ -promoted  $SrCo_0.4Fe_{0.6}O_{3-\delta}$ . Sep Purif Technol 2003;32(1):301–6. http://dx.doi.org/10.1016/S1383-5866(03)00046-7, Seventh International Conference on Inorganic Membranes, URL https://www.sciencedirect.com/science/article/pii/S1383586603000467.
- [37] Tong J, Yang W, Zhu B, Cai R. Investigation of ideal zirconium-doped perovskite-type ceramic membrane materials for oxygen separation. J Membr Sci 2002;203(1):175–89. http://dx.doi.org/10.1016/S0376-7388(02)00005-4, URL https://www.sciencedirect.com/science/article/pii/S0376738802000054.
- [38] Lv H, Jin Z, Peng R, Liu W, Gong Z.  $BaCo_xFe_{0.7-x}Zr_{0.3}O_{3-\delta}$  (0.2 $\leq x \leq$  0.5) as cathode materials for proton-based SOFCs. Ceram Int 2019;45(18):23948–53.
- [39] Zhang L, Shan J, Wang Q. BaCo<sub>0.4</sub>Fe<sub>0.4</sub>Zr<sub>0.2</sub>O<sub>3.-s</sub>: Evaluation as a cathode for ceria-based electrolyte IT-SOFCs. J Alloys Compd 2019;771:221–7. http://dx.doi.org/10.1016/j.jallcom.2018.08.232, URL https://www.sciencedirect.com/science/article/pii/S0925838818331207.
- [40] Zhang D, Zhang X, Zhou X, Song Y, Jiang Y, Lin B. Phase stability and hydrogen permeation performance of BaCo<sub>0.4</sub>Fe<sub>0.4</sub>Zr<sub>0.1</sub>Y<sub>0.1</sub>O<sub>3</sub>-δ ceramic membranes. Ceram Int 2022;48(7):9946–54.
- [41] Dwivedi SK, Schaefer L-A, Zeng Y, Sohn YJ, Malzbender J, Beyer A, et al. Design of a functional steam electrode for proton-conducting ceramic electrolysis cells based on BaCo<sub>0.4</sub>Fe<sub>0.4</sub>Zr<sub>0.2</sub>O<sub>3-δ</sub>: BaZr<sub>0.7</sub>Ce<sub>0.2</sub>Y<sub>0.1</sub>O<sub>3-δ</sub> composite. J Eur Ceram Soc 2025;117348.

- [42] Chen K, Jiang SP. Failure mechanism of (La,Sr)MnO<sub>3</sub> oxygen electrodes of solid oxide electrolysis cells. Int J Hydrog Energy 2011;36(17):10541-9. http://dx.doi.org/10.1016/j.ijhydene.2011.05.103, International Conference on Hydrogen Production (ICH2P)-2010, URL https://www.sciencedirect.com/science/article/pii/S0360319911013152.
- [43] Khan M, Xu X, Knibbe R, Zhu Z. Air electrodes and related degradation mechanisms in solid oxide electrolysis and reversible solid oxide cells. Renew Sustain Energy Rev 2021;143:110918. http://dx.doi.org/10.1016/j.rser.2021.110918, URL https://www.sciencedirect.com/science/article/pii/S1364032121002112.
- [44] Pan Z, Liu Q, Yan Z, Jiao Z, Bi L, Chan SH, et al. On the delamination of air electrodes of solid oxide electrolysis cells: A mini-review. Electrochem Commun 2022;137:107267. http://dx.doi.org/10.1016/j.elecom.2022.107267, URL https://www.sciencedirect.com/science/article/pii/S1388248122000698.
- [45] Yu X, Ge L, Wu B, Yu Z, He B, Jin Z, et al. Ultra durable composite steam electrode with cube-shaped BaZr 0.85 Y 0.15 O 3- δ facet-boosted efficiency toward advanced protonic ceramic electrolysis cells. J Adv Ceram 2025.
- [46] Løken A, Ricote S, Wachowski S. Thermal and chemical expansion in proton ceramic electrolytes and compatible electrodes. Crystals 2018;8(9):365.
- [47] Zhou C, Wang X, Liu D, Fei M, Dai J, Guan D, et al. New strategy for boosting cathodic performance of protonic ceramic fuel cells through incorporating a superior hydronation second phase. Energy Environ Mater 2024;7(4):e12660.
- [48] Duan C, Tong J, Shang M, Nikodemski S, Sanders M, Ricote S, et al. Readily processed protonic ceramic fuel cells with high performance at low temperatures. Science 2015;349(6254):1321–6. http://dx.doi.org/10.1126/science.aab3987, URL https://www.science.org/doi/abs/10.1126/science.aab3987.
- [49] Meng Y, Gao J, Huang H, Zou M, Duffy J, Tong J, et al. A high-performance reversible protonic ceramic electrochemical cell based on a novel sm-doped BaCe0· 7Zr0· 1Y0· 2o3-δ electrolyte. J Power Sources 2019;439:227093.
- [50] Ivanova ME, Escolástico S, Balaguer M, Palisaitis J, Sohn YJ, Meulenberg WA, et al. Hydrogen separation through tailored dual phase membranes with nominal composition BaCe0. 8Eu0. 2o3-δ: Ce0. 8Y0. 2o2-δ at intermediate temperatures. Sci Rep 2016;6(1):34773.
- [51] Rebollo E, Mortalo C, Escolástico S, Boldrini S, Barison S, Serra JM, et al. Exceptional hydrogen permeation of all-ceramic composite robust membranes based on BaCe 0.65 Zr 0.20 Y 0.15 O 3-  $\delta$  and Y-or Gd-doped ceria. Energy & Environ Sci 2015;8(12):3675–86.
- [52] Rosensteel WA, Ricote S, Sullivan NP. Hydrogen permeation through dense BaCe0. 8Y0. 2o3- δ-Ce0. 8Y0. 2o2- δ composite-ceramic hydrogen separation membranes. Int J Hydrog Energy 2016;41(4):2598–606.
- [53] Baharuddin NA, Abdul Rahman NF, Abd. Rahman H, Somalu MR, Azmi MA, Raharjo J. Fabrication of high-quality electrode films for solid oxide fuel cell by screen printing: A review on important processing parameters. Int J Energy Res 44(11):8296–313. http://dx.doi.org/10.1002/er.5518, arXiv:https://onlinelibrary.wiley.com/doi/pdf/10.1002/er.5518, URL https://onlinelibrary.wiley.com/doi/abs/10.1002/er.5518.
- [54] Fergus E, Hui R, Li X, Wilkinson DP, Zhang J. Solid oxide fuel cells: materials properties and performance. 1st ed.. CRC Press; 2008, http://dx.doi.org/10.1201/ 9781420088847.
- [55] Tan K, Rahman H, Taib H. Coating layer and influence of transition metal for ferritic stainless steel interconnector solid oxide fuel cell: A review. Int J Hydrog Energy 2019;44(58):30591–605. http://dx.doi.org/10.1016/j.ijhydene. 2019.06.155, Special Issue on the 6th International Conference on Fuel Cells and Hydrogen Technology (ICFCHT 2017), URL https://www.sciencedirect.com/ science/article/pii/S0360319919324553.
- [56] Somalu MR, Brandon NP. Rheological studies of nickel/scandia-stabilized-zirconia screen printing inks for solid oxide fuel cell anode fabrication. J Am Ceram Soc 2012;95(4):1220-8. http://dx.doi.org/10.1111/j.1551-2916. 2011.05014.x, arXiv:https://ceramics.onlinelibrary.wiley.com/doi/pdf/10.1111/j.1551-2916.2011.05014.x, URL https://ceramics.onlinelibrary.wiley.com/doi/abs/10.1111/j.1551-2916.2011.05014.x.
- [57] Jing J, Pang J, Chen L, Zhang H, Lei Z, Yang Z. Structure, synthesis, properties and solid oxide electrolysis cells application of Ba(Ce, Zr)O<sub>3</sub> based proton conducting materials. Chem Eng J 2022;429:132314. http://dx.doi.org/10.1016/j.cej.2021.132314, URL https://www.sciencedirect.com/science/article/pii/S1385894721038936.
- [58] Duan C, Kee R, Zhu H, Sullivan N, Zhu L, Bian L, et al. Highly efficient reversible protonic ceramic electrochemical cells for power generation and fuel production. Nat Energy 2019;4(3):230–40.
- [59] Toriumi H, Jeong S, Kitano S, Habazaki H, Aoki Y. Enhanced performance of protonic solid oxide steam electrolysis cell of Zr-rich side  $BaZr_{0.6}Ce_{0.2}Y_{0.2}O_{3-\delta}$  electrolyte with an anode functional layer. ACS Omega 2022;7(11):9944–50. http://dx.doi.org/10.1021/acsomega.2c00569.
- [60] Bauerle J. Study of solid electrolyte polarization by a complex admittance method. J Phys Chem Solids 1969;30(12):2657–70. http://dx.doi.org/10.1016/ 0022-3697(69)90039-0, URL https://www.sciencedirect.com/science/article/pii/ 0022369769900390.

- [61] Ebert JN, Jennings D, Schäfer L-A, Sebold D, Rheinheimer W. Bulk and grain boundary conductivity in doped BaZrO<sub>3</sub>: Bulk contribution dominates at operating temperatures. Scr Mater 2024;241:115852. http://dx.doi.org/10.1016/ j.scriptamat.2023.115852, URL https://www.sciencedirect.com/science/article/ pii/S1359646223005730.
- [62] Irvine JTS, Sinclair DC, West AR. Electroceramics: Characterization by impedance spectroscopy. Adv Mater 1990;2(3):132–8. http://dx.doi.org/10.1002/adma. 19900020304, arXiv:https://onlinelibrary.wiley.com/doi/pdf/10.1002/adma. 19900020304, URL https://onlinelibrary.wiley.com/doi/abs/10.1002/adma. 19900020304.
- [63] Lyagaeva JG, Vdovin GK, Medvedev DA. Distinguishing bulk and grain boundary transport of a proton-conducting electrolyte by combining equivalent circuit scheme and distribution of relaxation times analyses. J Phys Chem C 2019;123(36):21993–7. http://dx.doi.org/10.1021/acs.jpcc.9b05705.
- [64] Schneider CA, Rasband WS, Eliceiri KW. NIH image to ImageJ: 25 years of image analysis. Nature Methods 2012;9(7):671–5.
- [65] Huang Y, Merkle R, Maier J. Effects of NiO addition on sintering and proton uptake of Ba (Zr, Ce, Y) O 3- δ. J Mater Chem A 2021;9(26):14775–85.
- [66] Huang Y, Merkle R, Zhou D, Sigle W, van Aken PA, Maier J. Effect of Ni on electrical properties of Ba (Zr, Ce, Y) O3- $\delta$  as electrolyte for protonic ceramic fuel cells. Solid State Ion 2023;390:116113.
- [67] Wang B, Bi L, Zhao X. Exploring the role of NiO as a sintering aid in BaZr0. 1Ce0. 7Y0. 2o3- $\delta$  electrolyte for proton-conducting solid oxide fuel cells. J Power Sources 2018;399:207–14.
- [68] Sun H, Guo X, Li J, Li G, Yang Z, Ding H, et al. Effect of grain size on the electrical performance of BaZr<sub>0.1</sub>Ce<sub>0.7</sub>Y<sub>0.1</sub>Vb<sub>0.1</sub>O<sub>3-δ</sub> solid electrolytes with addition of NiO. Ceram Int 2019;45(1):622–6. http://dx.doi.org/10.1016/j. ceramint.2018.09.217, URL https://www.sciencedirect.com/science/article/pii/ S0272884218326828.
- [69] Liu Z, Wang X, Liu M, Liu J. Enhancing sinterability and electrochemical properties of  $\text{Ba}(\text{Zr}_{0.1}\text{Ce}_{0.7}\text{Y}_{0.2})\text{O}_{3-\delta}$  proton conducting electrolyte for solid oxide fuel cells by addition of NiO. Int J Hydrog Energy 2018;43(29):13501–11. http://dx.doi.org/10.1016/j.ijhydene.2018.05.089, URL https://www.sciencedirect.com/science/article/pii/S0360319918316057.
- [70] Tong J, Clark D, Bernau L, Sanders M, O'Hayre R. Solid-state reactive sintering mechanism for large-grained yttrium-doped barium zirconate proton conducting ceramics. J Mater Chem 2010;20:6333–41. http://dx.doi.org/10.1039/C0JM00381F.
- [71] Bonanos N, Steele B, Butler E, Macdonald JR, Johnson WB, Worrell WL, et al. Applications of impedance spectroscopy. Impedance Spectrosc: Theory, Exp Appl 2018;175–478
- [72] Yu S, Wang Z, Yang L, Liu J, Guan R, Xiao Y, He T. Enhancing the sinterability and electrical properties of BaZr<sub>0.1</sub>Ce<sub>0.7</sub>Y<sub>0.2</sub>O<sub>3</sub> – δ protonconducting ceramic electrolyte. J Am Ceram Soc 2021;104(1):329–42. http:// dx.doi.org/10.1111/jace.17467, arXiv:https://ceramics.onlinelibrary.wiley.com/ doi/pdf/10.1111/jace.17467, URL https://ceramics.onlinelibrary.wiley.com/ abs/10.1111/jace.17467.
- [73] Lyagaeva JG, Vdovin GK, Medvedev DA. Distinguishing bulk and grain boundary transport of a proton-conducting electrolyte by combining equivalent circuit scheme and distribution of relaxation times analyses. J Phys Chem C 2019;123(36):21993–7.
- [74] Saqib M, Lee JI, Park J-Y. BaCo $_{0.4}$ Fe $_{0.4}$ Zr $_{0.2}$ O $_{3-\delta}$  cathode materials for protonic ceramic fuel cells. ECS Trans 2019;91(1):1503. http://dx.doi.org/10.1149/09101. 1503ecst.
- [75] Somalu M, Yufit V, Shapiro I, Xiao P, Brandon N. The impact of ink rheology on the properties of screen-printed solid oxide fuel cell anodes. Int J Hydrog Energy 2013;38(16):6789–801.
- [76] Ji Q, Bi L, Zhang J, Cao H, Zhao XS. The role of oxygen vacancies of ABO 3 perovskite oxides in the oxygen reduction reaction. Energy & Environ Sci 2020;13(5):1408–28.
- [77] Somalu M, Yufit V, Brandon N. The effect of solids loading on the screen-printing and properties of nickel/scandia-stabilized-zirconia anodes for solid oxide fuel cells. Int J Hydrog Energy 2013;38(22):9500–10.
- [78] Somalu MR, Brandon NP. Rheological studies of nickel/scandia-stabilized-zirconia screen printing inks for solid oxide fuel cell anode fabrication. J Am Ceram Soc 2012;95(4):1220–8.
- [79] Kuai X, Yang G, Chen Y, Sun H, Dai J, Song Y, et al. Boosting the activity of BaCo0. 4Fe0. 4Zr0. 1Y0. 1O3- δ perovskite for oxygen reduction reactions at low-to-intermediate temperatures through tuning B-site cation deficiency. Adv Energy Mater 2019;9(38):1902384.
- [80] Duan C, Hook D, Chen Y, Tong J, O'Hayre R. Zr and Y co-doped perovskite as a stable, high performance cathode for solid oxide fuel cells operating below 500 C. Energy & Environ Sci 2017;10(1):176–82.